



AFRL-RQ-WP-TP-2020-0048

SHAPE OPTIMIZATION OF A LOW PRESSURE TURBINE CASCADE ENDWALL USING A GENETIC ALGORITHM

Christopher R. Marks, Jacob Dickel, and Rolf Sondergaard

**Turbomachinery Branch
Turbine Engine Division**

Mitch Wolff

Wright State University

**NOVEMBER 2019
Interim Report**

**DISTRIBUTION STATEMENT A. Approved for public release.
Distribution is unlimited.**

STINFO COPY

**AIR FORCE RESEARCH LABORATORY
AEROSPACE SYSTEMS DIRECTORATE
WRIGHT-PATTERSON AIR FORCE BASE, OH 45433-7542
AIR FORCE MATERIEL COMMAND
UNITED STATES AIR FORCE**

NOTICE AND SIGNATURE PAGE

Using Government drawings, specifications, or other data included in this document for any purpose other than Government procurement does not in any way obligate the U.S. Government. The fact that the Government formulated or supplied the drawings, specifications, or other data does not license the holder or any other person or corporation; or convey any rights or permission to manufacture, use, or sell any patented invention that may relate to them.

This report was cleared for public release by the USAF 88th Air Base Wing (88 ABW) Public Affairs Office (PAO) and is available to the general public, including foreign nationals.

Copies may be obtained from the Defense Technical Information Center (DTIC) (<https://discover.dtic.mil/>).

AFRL-RQ-WP-TP-2020-0048 HAS BEEN REVIEWED AND IS APPROVED FOR PUBLICATION IN ACCORDANCE WITH ASSIGNED DISTRIBUTION STATEMENT.

This report is published in the interest of scientific and technical information exchange and its publication does not constitute the Government's approval or disapproval of its ideas or findings.

REPORT DOCUMENTATION PAGE				<i>Form Approved</i> OMB No. 0704-0188	
<p>The public reporting burden for this collection of information is estimated to average 1 hour per response, including the time for reviewing instructions, searching existing data sources, gathering and maintaining the data needed, and completing and reviewing the collection of information. Send comments regarding this burden estimate or any other aspect of this collection of information, including suggestions for reducing this burden, to Department of Defense, Washington Headquarters Services, Directorate for Information Operations and Reports (0704-0188), 1215 Jefferson Davis Highway, Suite 1204, Arlington, VA 22202-4302. Respondents should be aware that notwithstanding any other provision of law, no person shall be subject to any penalty for failing to comply with a collection of information if it does not display a currently valid OMB control number. PLEASE DO NOT RETURN YOUR FORM TO THE ABOVE ADDRESS.</p>					
1. REPORT DATE (DD-MM-YY) November 2019		2. REPORT TYPE Interim		3. DATES COVERED (From - To) 01 May 2017 – 01 October 2019	
4. TITLE AND SUBTITLE SHAPE OPTIMIZATION OF A LOW PRESSURE TURBINE CASCADE ENDWALL USING A GENETIC ALGORITHM				5a. CONTRACT NUMBER In-house	
				5b. GRANT NUMBER	
				5c. PROGRAM ELEMENT NUMBER 61102F	
6. AUTHOR(S) Christopher R. Marks, Jacob Dickel, and Rolf Sondergaard (AFRL/RQTT) Mitch Wolff (Wright State University)				5d. PROJECT NUMBER 3002	
				5e. TASK NUMBER	
				5f. WORK UNIT NUMBER Q1BS	
7. PERFORMING ORGANIZATION NAME(S) AND ADDRESS(ES) Turbomachinery Branch (AFRL/RQTT) Turbine Engine Division Air Force Research Laboratory, Aerospace Systems Directorate Wright-Patterson Air Force Base, OH 45433-7542 Air Force Materiel Command, United States Air Force				8. PERFORMING ORGANIZATION REPORT NUMBER AFRL-RQ-WP-TP-2020-0048	
9. SPONSORING/MONITORING AGENCY NAME(S) AND ADDRESS(ES) Air Force Research Laboratory Aerospace Systems Directorate Wright-Patterson Air Force Base, OH 45433-7542 Air Force Materiel Command United States Air Force				10. SPONSORING/MONITORING AGENCY ACRONYM(S) AFRL/RQTT	
				11. SPONSORING/MONITORING AGENCY REPORT NUMBER(S) AFRL-RQ-WP-TP-2020-0048	
12. DISTRIBUTION/AVAILABILITY STATEMENT DISTRIBUTION STATEMENT A. Approved for public release. Distribution is unlimited.					
13. SUPPLEMENTARY NOTES PA Clearance Number: 88ABW-2019-4829; Clearance Date: 04 Oct 2019. This material is declared a work of the U.S. Government and is not subject to copyright protection in the United States.					
14. ABSTRACT Various approaches have been used to shape the endwall and blade profile in order to reduce the endwall losses in turbine passages. This study describes the workflow used to design an optimized endwall contour for a front-loaded high-lift low pressure turbine research profile. Endwall contours were defined using a series of Bezier curves across the passage to create a smooth contoured surface. A new computational mesh was generated for each design configuration by morphing the baseline mesh of a passage with a flat endwall until it matched each new contour shape. Two different contour designs were fabricated and installed in a low speed linear cascade wind tunnel to validate the workflow. One contour shape was designed using approaches described in open literature. The second shape was optimized using a genetic algorithm using passage total pressure loss as the objective function. The optimization process produced a unique and aggressive contour shape. Comparisons between the planar and the contoured endwall shapes are presented both experimentally and computationally. Although the two different contours produced a similar reduction in passage loss, the analysis shows that the effect of the two contours on the endwall flow field are significantly different providing insight into the fluid dynamic mechanism responsible for the reduction in endwall losses.					
15. SUBJECT TERMS endwall					
16. SECURITY CLASSIFICATION OF:			17. LIMITATION OF ABSTRACT: SAR	18. NUMBER OF PAGES 34	19a. NAME OF RESPONSIBLE PERSON (Monitor) Christopher R. Marks 19b. TELEPHONE NUMBER (Include Area Code) N/A
a. REPORT Unclassified	b. ABSTRACT Unclassified	c. THIS PAGE Unclassified			

TABLE OF CONTENTS

Section	Page
I. Introduction	1
II. Endwall Flow Description.....	3
III. Experimental Setup	5
IV. Design Methodology	7
A. Computational Flow Solver	7
B. Endwall Design Tool	9
C. Optimization Method.....	11
V. Shape Optimization Results	13
VI. Discussion of Computational Results.....	17
VII. Discussion of Experimental Results.....	20
VIII. Conclusions	23
Funding Sources.....	24
Acknowledgements.....	25
References.....	26
Nomenclature	29

LIST OF FIGURES

Figure		Page
Figure 1	Visualization of the time-averaged endwall flow structures through a low-speed linear cascade of high-lift, front loaded LP turbine blades.....	4
Figure 2	Top view of LSWT test section.	5
Figure 3	Baseline computational grid.	8
Figure 4	Grid independence study.	8
Figure 5	Design grid for an endwall containing six control curves.	9
Figure 6	Bezier curves with control points.	9
Figure 7	Transformed mesh grid with contour applied (design space).....	10
Figure 8	Original mesh grid with contour applied (physical space).	10
Figure 9	Sample binary string used to define the endwall contour.....	11
Figure 10	Generational mean and best contour shapes of generations 1 (a, e), 8 (b, f), 17(c, g), and 25 (d, h).	13
Figure 11	Standard deviation of endwall height of generations a.) 1, b.) 8, c.) 17, d.) 25.....	14
Figure 12	Generational average, elite population average, and cumulative best member with bars indicating one standard deviation of the population.	15
Figure 13	a.) Baseline endwall contour EWC1 compared with b.) GA optimized endwall contour EWC2 c.) EWC2 endwall height with significant topological features labeled as either a hill or valley.	16
Figure 14	Iso-surfaces of $Q = 10$ colored by secondary vorticity rotational direction, with streamlines seeded in the boundary layer a.) planar endwall b.) EWC1 c.) EWC2.	17
Figure 15	Numerical predictions of total pressure loss coefficient distribution plotted with iso-surfaces of $Q = 10$ for a.) planar, b.) EWC1, c.) EWC2.....	18
Figure 16	Downstream loss distribution in the 150% C_x plane a.) planar endwall b.) EWC1 c.) EWC2 d.) pitchwise integrated wake total pressure loss coefficient.....	18
Figure 17	Experimental total pressure loss coefficient distribution through the exit and downstream of the passage for the a.) planar b.) EWC1 c.) EWC2 endwall shapes.....	20
Figure 18	Pitchwise integrated wake total pressure loss coefficient in the 150% C_x plane a.) experiment b.) computational model.	21
Figure 19	EWC2 total pressure loss coefficient distribution through the exit and downstream of the passage for a.) computational simulation and b.) experimental.	21

I. Introduction

The aerodynamic performance of the Low-Pressure Turbine (LPT) section is vital to the overall capability, size, weight, and cost of aircraft gas turbine engines. In high-bypass turbofan engines, the LPT-driven fan powers as much as 80% of the engine thrust and can account for nearly a third of the overall engine weight [1]. In order to achieve large pressure ratios, the LPT section can contain over 1000 individual airfoils [2]. Technology improvements that enable design trades on power extraction for a given size, weight, and part count are a focus of research in the LPT section. A key design parameter that drives the size and part count in the LPT section is the blade aerodynamic loading level. As the loading level of individual blades in the turbine are increased, fewer blades are required to extract the same amount of power from the flow. Aerodynamic loading is directly related to airfoil curvature. As the curvature is increased, the adverse pressure gradients on the suction surface grow. At low Reynolds number operating conditions, the blade suction surface boundary layer can separate due to the strong adverse pressure gradient, severely degrading performance. High-lift blade profiles that perform well at low Reynolds numbers have been designed by using front-loaded pressure distributions Refs. [2,3], but performance in the endwall region is typically neglected for midspan design purposes [3]. The work of Schmitz et al. [4], which included full stage rotating experiments, showed that rigorous physics-based design processes can be used to produce a high-load stage geometry that meets performance goals. A challenge remains in the endwall region where increased loading levels can lead to high endwall losses. The complex flow interactions and loss generation at the junction of the blade and endwall are difficult to predict numerically. Techniques to mitigate endwall losses and validated numerical tools to design and predict their benefit are necessary to increase LPT blade loading in aircraft engines.

Various approaches to reduce losses and improve blade performance in the endwall region can be found in the literature. These techniques include passively shaping the blade and/or endwall geometries; or actively controlling the momentum along the endwall and blade surfaces to manipulate the secondary flow and reduce losses. Examples of active approaches can be found in Refs. [5-7] amongst others.

Passive approaches to improve endwall aerodynamics range from the addition of fence-like structures to full three-dimensional shaping of the junction flow region. Kawai et al. considered the size and location of fences placed on the endwall [8] and provided visualization of the secondary flow with and without the fences installed [9]. The work showed that optimal fences must be small relative to boundary layer thickness and positioned to trap the pressure side leg of the horseshoe vortices reducing their interaction with the blade surface [8]. Chung et al. [10] investigated an endwall fence in a cascade simulator to improve film cooling effectiveness. In their configuration, the addition of the endwall fence reduced the strength of the endwall vortical flow and moved it further away from the suction surface, reducing the aerodynamic losses associated with the endwall flow. Aunapu et al. [11] implemented a similar fence to the one described in [10], then replaced the fence with a row of steady jets. They found that the jets could divert the path of the passage vortex, however the jets increased the aerodynamic losses in the passage.

Modifications to the shape of the blade junction with the endwall have also been shown to influence the secondary flow. The work of Sauer et al. [12] showed that thickening the leading edge of the blade very close to the endwall, referred to as a leading edge endwall bulb, strengthened the suction side leg of the horseshoe vortex affecting endwall vortices strengths and interactions, and reducing overall secondary losses. Lyall et al. [13] showed that the endwall

losses of a front-loaded high-lift blade can be reduced by contouring the blade shape near the endwall with a low stagger angle profile. Decreasing the stagger angle near the endwall reduced the strength of secondary flow vortices and compressed their effect toward the endwall, reducing aerodynamic losses [14].

While effective, shape contouring at the junction with the endwall uses a limited portion of the available design space in a turbine passage. Another approach is to three-dimensionally shape the entire endwall region between the blades by strategically adding hills and valleys. Three-dimensional contouring is typically referred to as non-axisymmetric endwall contouring. Early research in this area includes the paper by Atkins [16] who applied non-axisymmetric endwalls in a linear cascade and found an increase in losses. Rose [17] designed non-axisymmetric endwalls to improve the circumferential uniformity of the static pressure field in a nozzle guide vane and thus reduce rim seal leakage. Their design approach used streamline curvature to modify the static pressure field. Many detailed studies followed these early works with a focus on reducing negative effects of endwall flows, making endwall contouring an active research area for nearly two decades. Studies in linear cascades through rig testing have shown that contouring of the endwall can significantly reduce passage losses (e.g., Refs. [17-22]). Praisner et al. [22] performed a study on high-lift ($Z_w=1.4$) and conventional-lift blades with and without non-axisymmetric endwall contouring to compare the benefits of using endwall contouring. Ultimately, the study was an attempt to reduce the losses of the high-lift blades to the same level of the conventional lift blade [22]. The endwall contours were produced in an optimization routine using sequential quadratic programming with the design goal of reducing row total pressure loss. They found non-axisymmetric contouring had less benefit on an aft-loaded blade compared to a front-loaded blade and that the contour for the front-loaded, high-lift airfoil had a more extreme shape compared to the aft-loaded airfoil [21].

The studies mentioned above show that both blade profile and endwall contouring are methods capable of reducing endwall losses through high-lift blade passages. Design approaches that optimally shape both the blade profile and endwall contour will be most effective at reducing endwall loss through the passage. Development of these complicated three-dimensional shapes require both a better fundamental understanding of how these contouring approaches reduce aerodynamic losses and accurate numerical design tools.

This investigation details the numerical tools, workflow, design and experimental validation of endwall contours for the front loaded high-lift (L2F) research profile. Two endwall contours were developed and tested in a low speed linear cascade wind tunnel. The first contour was designed based on approaches described in the open literature, while a second contour was designed using a genetic algorithm to develop an optimized contour based on a minimization of passage total pressure loss coefficient. The optimization process produced an aggressive endwall shape compared to the first shape. Detailed experimental measurements are compared with numerical simulations validating the design methodology and providing insight into the fluid dynamic mechanism responsible for the reduction in endwall losses.

II. Endwall Flow Description

The turbine flow field has been examined and described by many researchers (e.g., Ref. [23]). Several vortical structures are present in both conventional lift and high lift airfoils. At the junction of the blade and endwall, the incoming boundary layer (BL) approaches the leading edge creating an adverse pressure gradient. The BL then separates and rolls-up into what is typically described as a horseshoe vortex (HV) structure. The HV wraps around the leading edge of the airfoil forming two legs denoted by the respective half of the passage in which the vortex resides (i.e., pressure side (PS) and suction side (SS)). The pressure side leg of the HV extends across the passage forming what is referred to as the passage vortex (PV). The vortices in the endwall region interact with each other in the downstream half of the passage generating losses. Additional vortices in the endwall region of turbine blades include corner separations and the trailing edge shed vortex. The latter vortex forms in the wake of the blade due to the spanwise change of the blade circulation [24].

This study details endwall shape optimization of the L2F LPT research profile. The L2F is a front-loaded, high-lift, airfoil with the same design gas angles as the Pratt & Whitney Pack B research airfoil, 35° and 60° for the inlet and exit angles, respectively [3]. The L2F has a design Zweifel loading level of 1.59 compared with 1.15 for the Pack B. The peak loading location is near 25% axial chord resulting in a more gradual pressure recovery along the remainder of the blade suction surface. At the midspan location, the L2F has excellent Reynolds-lapse in total pressure loss compared to similarly loaded blades with more aft loaded pressure distributions [3,13].

Several recent investigations [7,13-15,25-27] of high-lift LPT endwall aerodynamics have been accomplished using the L2F geometry in a low-speed linear cascade wind tunnel. An accompany Implicit Large Eddy Simulation (ILES) has been developed and described in Gross et al., [28]. Detailed comparison of the simulation and experimental measurements showed excellent agreement in both velocity distribution and loss generation [15,28]. The experiments and simulation together provided a detailed understanding of the time-averaged endwall flow structures and loss generation through the passage.

Visualization of the time-averaged endwall flow using the results from the ILES is shown in Figure 1.

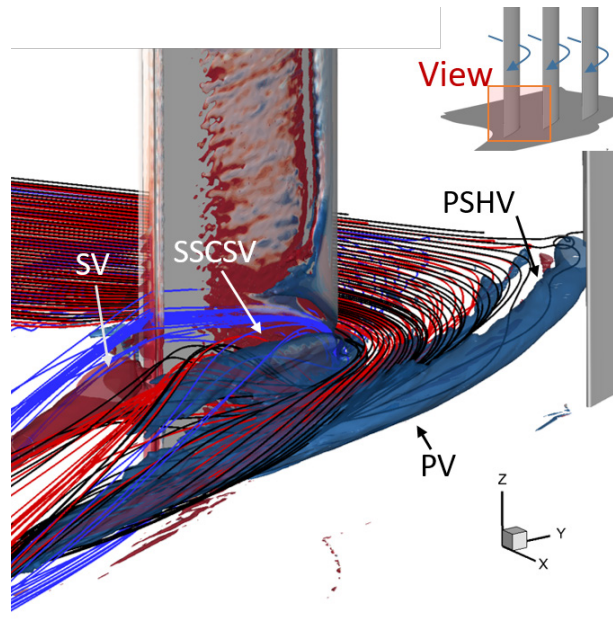


Figure 1 Visualization of the time-averaged endwall flow structures through a low-speed linear cascade of high-lift, front loaded LP turbine blades.

The Reynolds number of the numerical simulation is 100,000 based inlet velocity and blade axial chord. The image perspective is from downstream viewing into the passage upstream towards the suction side trailing edge. Isosurfaces of Q-criterion show the dominant vortical structures within the passage of the L2F. The isosurfaces have been colored by secondary vorticity to indicate the rotational direction. Blue reflects a clockwise (relative to the view) or negative rotation in the axial direction. The red isosurfaces represent counterclockwise or positive rotation flow in the axial direction. Three sets of streamlines were seeded from points located at 1.8%, 18%, and 36% of the boundary layer thickness and are colored, blue, red, and black respectively.

The visualization in Figure 1 shows several significant three-dimensional endwall structures through the front loaded passage. The pressure side leg of the horseshoe vortex (PSHV), formed at the junction of the blade leading edge and endwall, extends across the passage under the influence of the cross-passage pressure gradient. The PV structure is strengthened and fed by the secondary flow across the passage. The PV interacts with a strong corner separation and vortical structure originating along the blade suction surface near the pressure minimum and extending toward the trailing edge. The vortical structure has the same direction of rotation as the PV and is referred to as the suction side corner separation vortex (SSCSV). The low momentum flow along the wall of the incoming boundary layer (blue streamlines) is entrained in both the SSCSV and along the suction surface in the corner separation region marking the furthest extend of the endwall flow up the suction surface. The interaction between the PV, corner separation, and free stream flow in the corner region generates significant losses. The trailing edge shed vortex (SV) is formed in the wake of the blade and has an opposite sense of rotation compared to the SSCSV and PV. The suction side leg of the horseshoe vortex is not visible in this view, it is weak relative to the other features and is only noticeable in the front portion of the passage. A thin, closed laminar separation bubble forms on the suction surface at low Reynolds numbers. The endwall flow structures and loss generation are described in more detail in Refs. [14,28].

III. Experimental Setup

AFRL's Low Speed Wind Tunnel (LSWT) Facility was used for experimental verification of the numerical prediction tools. The wind tunnel test section is configured as a low-speed linear cascade with seven L2F blades, as shown in Figure 2.

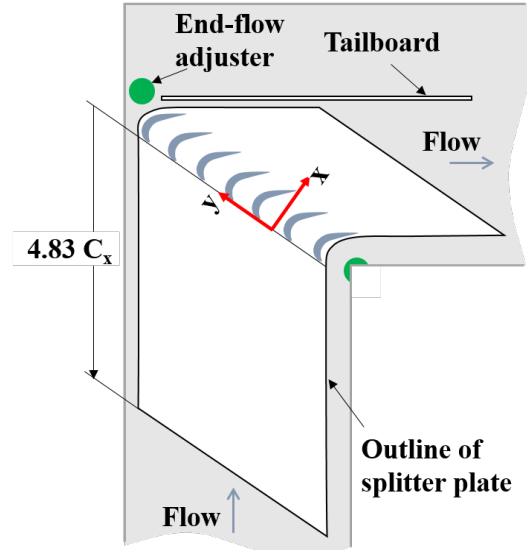


Figure 2 Top view of LSWT test section.

A turbulence grid installed upstream of the test section increased the free stream turbulence intensity (FSTI) to 3.1%. A splitter plate was used to create an artificial endwall with a clean incoming BL. The splitter plate surrounded the blades and extended upstream and downstream of the blade row. The passage had a relatively large AR of 4.17 to differentiate the flows in the endwall region from the two-dimensional flow at mid-span. The splitter plate configuration results in a BL thickness of 2.2% span (9.3% C_x) at a Reynolds number of 1.0×10^5 based on inlet velocity and axial chord. Table 1 summarizes these quantities.

Table 1 Linear cascade dimensions and flow properties.

Number of Blades	7
Axial Chord (C_x)	6 [in]
Pitch/Axial Chord (S/C_x)	1.22
Span/Axial Chord (H/C_x)	4.17
Re_{C_x}	1.0×10^5
Boundary Layer Thickness ($\delta_{99\%}$)	0.56 [in]
Free Stream Turbulence Intensity (FSTI)	3.1%

The contoured endwalls were printed out of plastic using an additive manufacturing technique. They were created in several pieces so that the endwall could be reconfigured as a flat or contoured endwall without removing the blades from the cascade.

Several 0-1 inch H_2O All Sensors transducers were used to measure the total pressure loss between an upstream pitot static probe and downstream Kiel probes in a custom five probe rake. A single, custom inline Kiel probe was used for in-passage total pressure loss measurements. A 0-0.4 inch H_2O Druck pressure transducer connected to a Pitot-static probe located two axial

chords upstream was used to measure the incoming dynamic pressure. The incoming dynamic pressure was used to set the tunnel velocity. All pressure transducers were calibrated with a Ruska 7250 low pressure calibrator. A traverse was used to move the downstream Kiel probes and obtain measurements in a two-dimensional grid. Area averaged values of passage total pressure loss coefficient were calculated in a downstream measurement plane ($1.5 \cdot C_x$ from the blade leading edge) by first integrating in the pitchwise direction, and then in the spanwise direction. The pitchwise and spanwise integrals were non-dimensionalized by the pitch and span lengths, respectively.

IV. Design Methodology

Optimization of LPT turbines requires a robust system capable of modeling the complex flow through blade rows comprised of numerous design variables. In this study, endwall contours are developed for a passage of the low speed linear cascade of L2F research profiles. An optimization workflow was developed to generate endwall contour shapes, manipulate the baseline computational mesh to match the new endwall shape, compute, and post-process results from the flow solver.

The following sections provide further description of the endwall design tool and implementation of the genetic algorithm used for shape optimization.

A. Computational Flow Solver

For design purposes, the flow through the cascade passage was modeled using three-dimensional Reynolds-averaged Navier-Stokes simulations facilitated by the commercial flow solver Code Leo, with structured meshes facilitated by Code Wand. The flow solver is described in [29]. It is a density-based time-marching code that employs cell vertex finite volume approximations to the conservation laws of mass, momentum, and energy that are second order accurate in space and time [29]. The flow solver has been used to model the flow through the low speed linear cascade passage for design purposes [13]. The solution was compared with experimental measurements in [14]. Together, good agreement was found in terms of the numerical technique capturing the changes in the endwall flow when various blade profile shapes were used at the junction of the blade and endwall.

A steady simulation was performed with an incoming Reynolds number of 1.0×10^5 to match the experiments. The inlet Mach number of the experiments was 0.03, well within the incompressible regime. The Mach number of the simulations was increased to 0.15, to reduce the stiffness of the governing equations and accelerate convergence, while remaining incompressible. The Mach number was adjusted by changing the inlet total pressure and static pressure at the exit in order to maintain the desired inlet velocity and Reynolds number.

Turbulent viscosity for the fluid flow was determined using Wilcox's two-equation $k-\omega$ turbulence model [30]. An evaluation of the effect of the inlet turbulence parameters when utilizing the $k-\omega$ turbulence model as implemented in the flow solver was detailed in [31]. When the experimental values of incoming turbulence were specified at the inlet plane, there was a significant overprediction of profile total pressure loss. The predicted total pressure loss was found to be highly sensitive to the specified integral length scale, which does not necessarily match the physical scales present in the flow. In the current simulations the inlet turbulence intensity was set to 1% and integral length scale to $0.0017 C_x$ following the recommendation in [31]. As with other RANS simulations, the predicted results should not be considered in terms of absolute accuracy. The simulations will be shown later to provide good agreement of the endwall flow structures with the experiments, including the relative improvement in total pressure due to various degrees of endwall shaping.

One full pitch of the linear cascade was simulated. The baseline computational grid is shown in Figure 3.

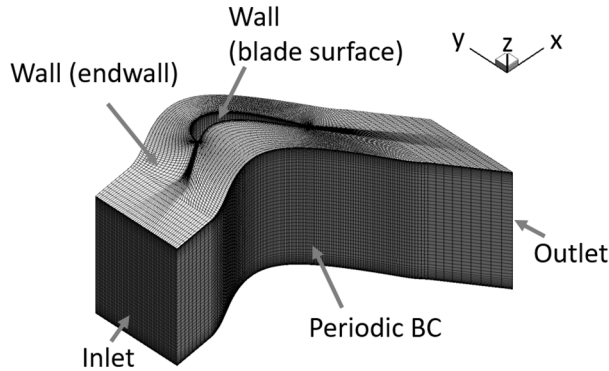


Figure 3 Baseline computational grid.

A structured multi-block mesh consisting of an O-grid around the blade surface, and H-grids for the remainder of the domain, were used to discretize the domain. The mesh topology is referred to as OHH as additional H-grids were used to provide sufficient resolution to capture flow phenomena near the leading and trailing edges.

The baseline passage flow simulation used the same flow solver and meshing process previously used to model blade endwall contour shapes [13,14], providing confidence in the use of the numerical flow simulation for endwall contour design. A grid independence study was conducted using the grid for the baseline case with a planar endwall. Grid independence was evaluated by monitoring the change in the downstream total pressure loss as mesh resolution was varied. The total pressure loss coefficient is a direct indicator of numerical dissipation due to the grid [32, 31] and is used in the subsequent endwall shape optimization as an objective function. The results of the grid independence study is shown in **Figure 4**.

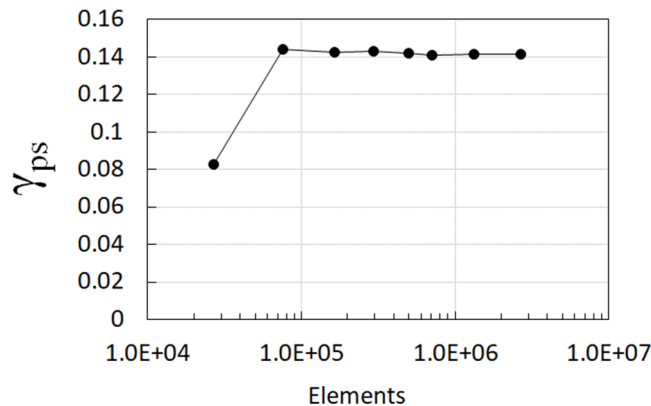


Figure 4 Grid independence study.

The pressure loss coefficient converged rapidly as the number of elements were increased beyond 1.65×10^4 , with a maximum difference of 2.4% as the number of points were increased to as high as 2.7 million. The study shows that the solution is essentially grid-independent when a mesh size of 501,760 elements is used. All simulations were run at one level finer mesh, consisting of 712,704 elements. This value was chosen as it balanced the requirement of using a sufficient grid resolution to capture the necessary flow physics, while minimizing computational cost – a critical balancing act when the flow model is incorporated into an evolutionary based optimization strategy. The solution was considered to be converged when the largest average

change in density and conservative variables had decreased by five orders of magnitude. This typically occurred within 4000 iterations. These findings are consistent with a prior related study described in [13, 31].

B. Endwall Design Tool

A numerical tool was created to generate contoured endwall surfaces based on an initial (baseline) planar (or radial) endwall. The initial planar endwall was generated on a structured grid facilitated by Code Wand. The contoured endwalls for this study were generated using a design grid with a small number of control curves. The steps to create the non-axisymmetric endwall contour are shown in Figures 5 through 8.

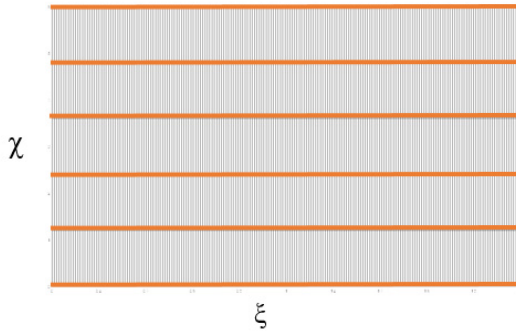


Figure 5 Design grid for an endwall containing six control curves.

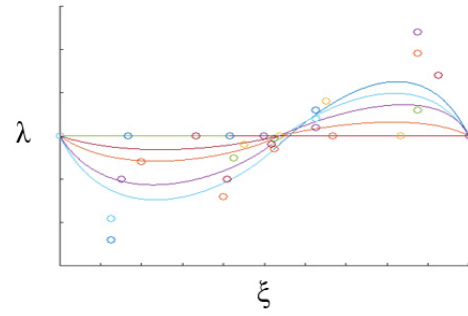


Figure 6 Bezier curves with control points.

An example of a design grid is shown in Figure 5 - six control curves extend across the pitch of the passage at six different axial positions. This design grid is the foundation on which each non-axisymmetric endwall contour is built upon. A series of Bezier curves (shown in Figure 6) are used to define the contoured endwall shape. These Bezier curves act as the control curves in the design grid. There are a total of six curves shown, but only the four interior planes were used to generate a contoured endwall shape. The two at the inlet and exit of the passage were held at a zero spanwise height. The general equation for a cubic Bezier curve is:

$$\mathbf{B} = (1 - t)^3 \mathbf{P}_0 + 3(1 - t)^2 t \mathbf{P}_1 + 3(1 - t) t^2 \mathbf{P}_2 + t^3 \mathbf{P}_3, \quad 0 \leq t \leq 1 \quad (1)$$

where \mathbf{P}_i in Equation 1 are the control points for the Bezier curve, t is a parametric independent variable ranging from zero to one, and \mathbf{B} contains the coordinates for the curve itself. This vector equation defines both the pitchwise (ξ) and spanwise (λ) coordinates in the design grid. The spacing between the control curves defines the axial coordinates of the curves. The main objective of the design grid is to specify the respective height (spanwise values) for the computational grid used in the flow solver. Cubic Bezier curves were chosen based on maximizing the possible contour shapes while minimizing the number of variables.

For added flexibility in the design space, two Bezier curves were used per axial plane. This allowed localized influence on the endwall shape at more points across the pitch. Each Bezier curve smoothly transitioned into another by holding the slope between two curves the same. This slope was dependent on the two respective control points on either side of the connection point.

Once the height is specified on the design grid, the mesh grid is transformed to the coordinate system of the design grid. This conversion from real coordinates to the design space is a

straightforward transformation of the real coordinates into a rectangular grid. Once both the design grid and mesh grid are in the same coordinate system, a cubic interpolation is performed to apply the contour from the design grid to the mesh grid points (Figure 7). Finally, the mesh grid is converted back into the real coordinates and the non-axisymmetric endwall contour is obtained (Figure 8).

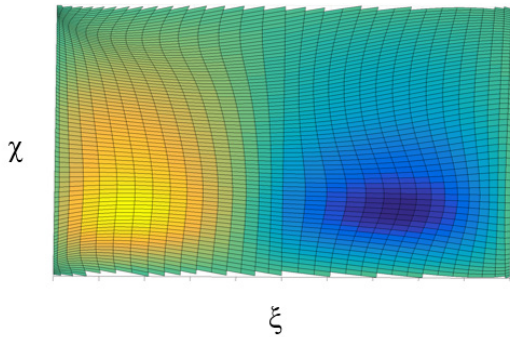


Figure 7 Transformed mesh grid with contour applied (design space).

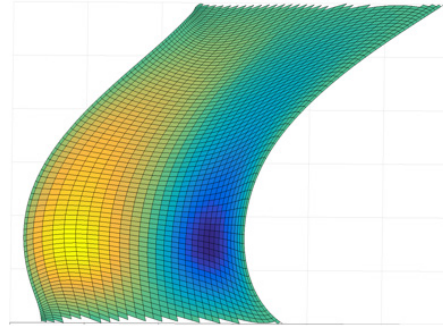


Figure 8 Original mesh grid with contour applied (physical space).

Figure 8 shows a design contour applied to the original mesh coordinates. A mesh morphing tool (MORPH [34]) was used to deform the grid independent planar endwall of the baseline 3-D mesh into the contoured surface. The MORPH code uses a spring analogy to deform the mesh resulting in a high-quality deformed mesh with minimal skewing of cells [34]. The code iterates until the average mesh quality is above a certain threshold or until a maximum number of iterations is reached.

An initial non-axisymmetric endwall contour (designated EWC1) was designed with the aforementioned tools to verify that the process could be used to develop a contour with reduced losses. The EWC1 contour was produced using a gradient-based approach utilizing total pressure loss in the downstream plane as a cost function. The intent of the shape was to force low-speed flow near the LE of the endwall toward the SS of the blade before it enters the passage in order to decrease the size, strength, and trajectory of the PS leg of the HV and downstream PV. The overall effect is a reduction in the strength of PV and its interaction with the corner separation and SS flow. The EWC1 shape was fabricated and tested in the low-speed linear cascade wind tunnel for experimental validation. Discussion of the EWC1 numerical model and experiment are combined with the optimized contour in later sections.

After verifying that the design tools capture the flow phenomena adequately, a binary genetic algorithm (GA) method was developed to produce an optimized non-axisymmetric endwall contour, designated EWC2. The algorithm was similar to the turbine vane film-cooling optimization described in Johnson et al. [33]. Generational methods, like GA and particle swarms, are commonly used for complex optimization problems. GAs obtain an optimum configuration by determining the fitness of each design case and retaining the best genetic material from each generation to populate the next. The genetic material in the context of design takes the form of design parameters. The fitness value for each of the members of a generation are calculated and weighted by the probability that a member will pass on its genetic material. The transfer of genetic material is similar to the passing of genes of the parents to offspring in nature [35]. Genes from each parent crossover with an allowance for mutation. A diverse initial

population is required to find a global extrema and reduce the chance of arriving at a local minimum or maximum. As the design evolves from generation to generation an optimal solution is developed. A drawback of the evolutionary based approach is the high computational cost associated with evaluating a large number of design cases. The advantages of a GA are that they are easily implemented, have been shown to reliably find a global optimum in n-dimensional optimization problems, and provide insight on design parameters by showing which are critical and which are not. The following subsection describe the optimization routine.

C. Optimization Method

Binary-encoded GAs have been shown to be reliable and efficient at finding a global optimum [33]. Binary digits are restricted to a value of either “0” or “1”, which means that every additional digit used to represent a variable will increase the total number of design cases by a factor of two. A total of 224 binary digits were used in the endwall shape optimization with $2.70E^{67}$ possible design cases.

A total of 40 variables were used in the optimization to control the shape of the endwall contour. Sixteen of the variables corresponded to the pitchwise location of the various control points. In Figure 6, these variables correspond to the ξ -direction, represented by five bits each in the binary string. The twenty-four other variables correspond to the spanwise height in the λ -direction. The spanwise control points were represented by six bits each in the binary string. The values could vary between zero and one for the pitchwise locations and from -1.5 to 1.5 for the spanwise locations, which corresponds to one pitch and $\pm 6\% H$ ($\pm 25\% C_x$), respectively. Higher bit counts could be used for additional discrete design cases, but the current bit size for each variable was sufficient. Increasing the number of bits per design point would increase the complexity of the design problem. There would be diminishing returns by increasing the bit count and maintaining the same design bounds.

Figure 9 shows a portion of a binary string defining an entire contour shape. This portion shows the boundary in the string where the pitchwise and spanwise control points meet. The five-digit and six-digit segments represent the pitchwise and spanwise control points, respectively.

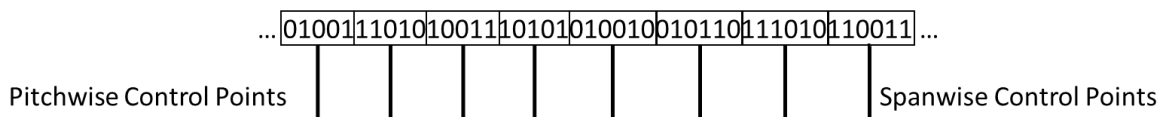


Figure 9 Sample binary string used to define the endwall contour.

Uniform, two point, and single point crossover were used to pass genetic material (design parameters) from one generation to the next. The percentages of each crossover type were 70%, 20%, and 10%, respectively. The percentages represent the probability of each crossover type being applied after two parents were selected for the reproduction of the next generation. A weighted roulette wheel with a mutation rate of 0.1% was used as the selection criteria style. All the designs available for the selection process had a slice on the roulette wheel and the size of that slice was dependent on the design’s fitness value. Fitness values were used as a feedback function in the algorithm denoting definitive criteria for good and bad designs. The weighting of the roulette wheel for this study was based on the fitness value of total pressure loss, γ_{ps} . Design configuration’s with a small value of γ_{ps} had a higher probability of being chosen for crossover, mutation, and passing on their genetic material compared to designs with higher γ_{ps} .

Mutation occurred by randomly switching a binary digit based on the rate supplied. Each binary digit for every member in a generation was given a random number between 0-100. Mutation occurred if the random number was below the specified mutation rate. For example, if the random number for a binary digit was 5 and the mutation rate is 0.1, mutation would not occur. If the random number was 0.05 with the same mutation rate, mutation would occur. At a mutation rate of 0.1% and 224 binary digits per member, approximately 0.224 binary digits were changed per member. The result was approximately one binary digit would be changed per every four members in the generation, or 22 per generation. As mutation was random at the specified rate, the occurrence of mutations for multiple binary digits per member was possible.

Elitism was used to accelerate optimum convergence by eliminating the weakest members in a generation and having a pool of elite optimization members for crossover and mutation. Appropriate restrictions on the Bezier control points were used to reduce the chance of a non-physical design occurring; e.g. a Bezier curve looped back on to itself. Duplicate members were also excluded from participating in any generation, as they would provide no new information. Any duplicates were rejected, and a new member was created using the same process at the other members of the generation. Checks for duplicates were performed at the time a member was created to reduce any interference with creating a new generation.

The initial population of 100 contour designs was produced using Latin Hypercube Sampling (LHS) to create a diverse set of genetic material for the algorithm. The initial generation was used in its entirety to create the second generation in the optimization process ensuring that the most elite 100 members of the entire optimization were used to create the next generation. Generation 2 and on used the cumulative elite (best 100 members) for crossover and mutation. This approach can lead to skewed optimization results but can also accelerate convergence toward a particular optimal design. Some negative effects of elitism include the elimination of vital genetic material that results in obtaining only local extrema instead of the global extrema that is desired. This risk was taken into consideration and elitism was used with the purpose of retaining beneficial genes to accelerate convergence.

V. Shape Optimization Results

The focus of the optimization was on reducing the total pressure loss through a passage of the linear cascade. The area averaged total pressure loss coefficient in the downstream plane was used as the cost function. The endwall design shape evolved over the course of 25 generations inside of the optimization routine, requiring the analysis of over 2500 unique design shapes.

The generational mean and standard deviation of the endwall surface shape was calculated as the design evolved. Figure 10 shows the respective mean spanwise displacement for the endwall of generations 1, 8, 17, and 25.

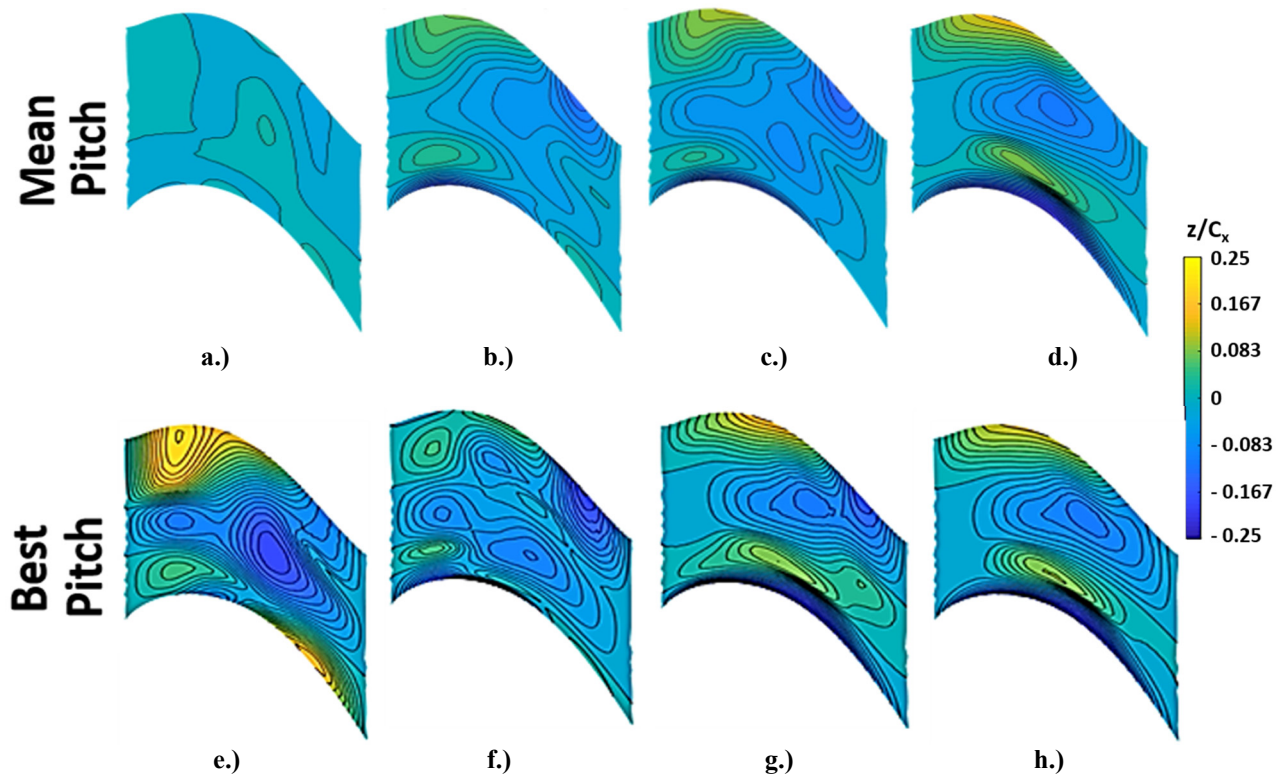


Figure 10 Generational mean and best contour shapes of generations 1 (a, e), 8 (b, f), 17(c, g), and 25 (d, h).

The best contour shape for the four generations is also shown. The mean displacement of generation one is close to zero everywhere, which indicated there was no major bias induced from the initialization process. It should be noted that the first generation's best case resulted in an increase in total pressure loss when compared to the baseline case. The mean and best contours of the subsequent generations illustrate the evolution of the endwall shape over the progression of the optimization. The standard deviation of the spanwise displacement of the endwall over select generations are shown in Figure 11.

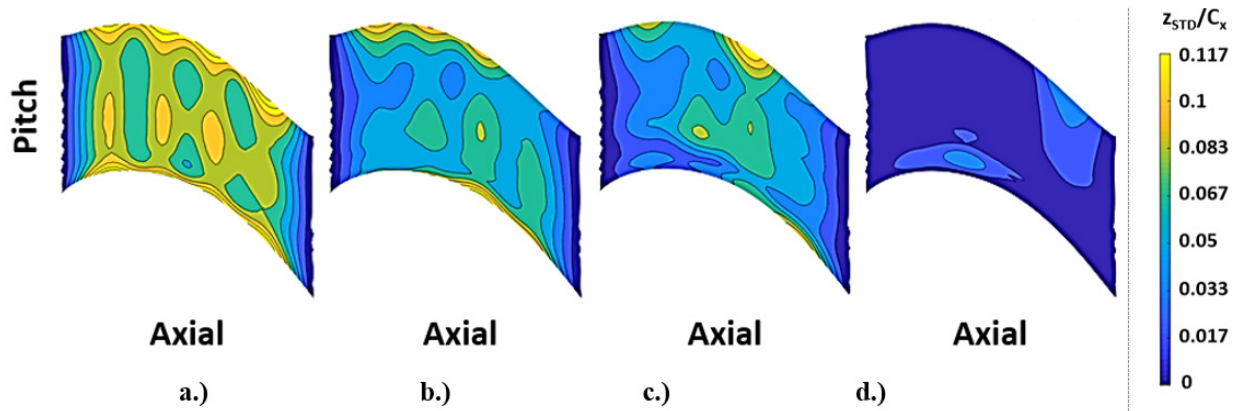


Figure 11 Standard deviation of endwall height of generations a.) 1, b.) 8, c.) 17, d.) 25.

The plots show the region of the endwall at which the shape was most significantly varied or refined during that generation of the optimization. During generation one (Figure 11a), the locations of the Bezier curves are prominent, with large standard deviations indicating significant variation of the shape due to the diverse initial population. The shape of the endwall at the inlet and exit of the passage were fixed boundary regions allowing the flat endwall outside the passage to smoothly transition into a contoured surface inside the passage. This region had the smallest standard deviation and shape variation in the passage throughout the generations. As the design evolved the standard deviation decreased as the population narrowed into a subset of the design space. The regions with elevated standard deviation highlight areas where the shape was varied by the algorithm to further reduce the cost function. In generation 17 (Figure 11c), the optimization algorithm was converging upon the height near the pressure side of the blade along with a region slightly off the suction side of the blade 40% to 60% axial chord downstream. By generation 25, there were only two regions of the endwall that were still under refinement.

It should be noted that using additional control curves would result in more control over the contour shape. Based on the large standard deviation across the endwall, the six control curves (four non-zero curves) inside the passage were considered sufficient to allow significant exploration of the design space and arrive at an optimum contour.

The progression of the cost function over each generation is summarized in Figure 12 which illustrates the generational averages with bars of one standard deviation. As the generations progressed, the standard deviation decreased. This figure also shows the evolution of the average of the elite population and its respective standard deviation. The standard deviation of the elite population decreased quicker than the average of the entire generation, and the elite average value steadily decreased throughout the optimization process. The cumulative best member is also plotted along with the baseline planar case for reference.

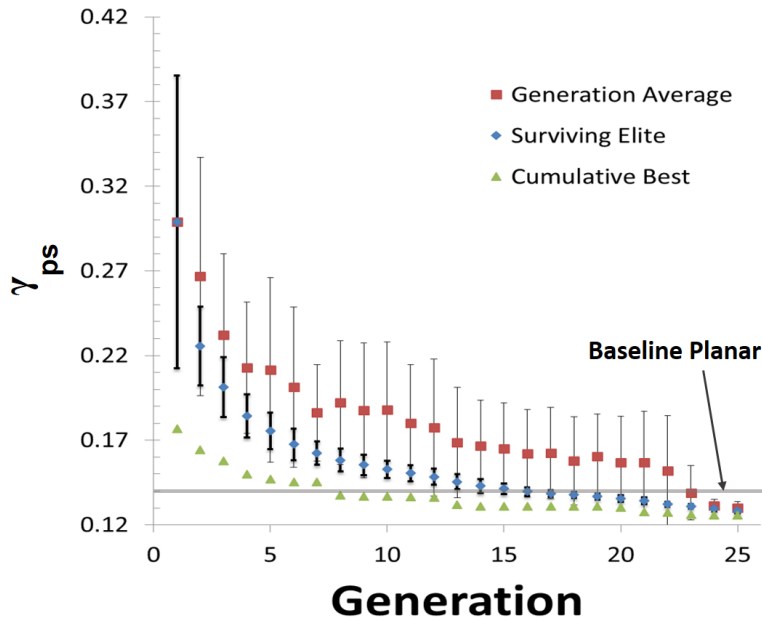


Figure 12 Generational average, elite population average, and cumulative best member with bars indicating one standard deviation of the population.

Between generations 14 and 19 there was little change in the passage total pressure loss of the overall cumulative best member, however, the elite average and generation averages steadily decreased. In order to accelerate convergence toward an optimal design configuration, the weighting on the roulette wheel selection was increased beginning in generation 19. This change resulted in the additional improvement in cumulative best passage total pressure loss until generation 23 at which point the cumulative best stabilized and the averages of the generation and elite population rapidly approached the cumulative best.

The optimization process was stopped after the 25th generation. Figure 13 shows the best contour shape, referred to as EWC2, produced by the optimization routine compared with the baseline contour EWC1. The shaping of the surface is complex with large gradients.

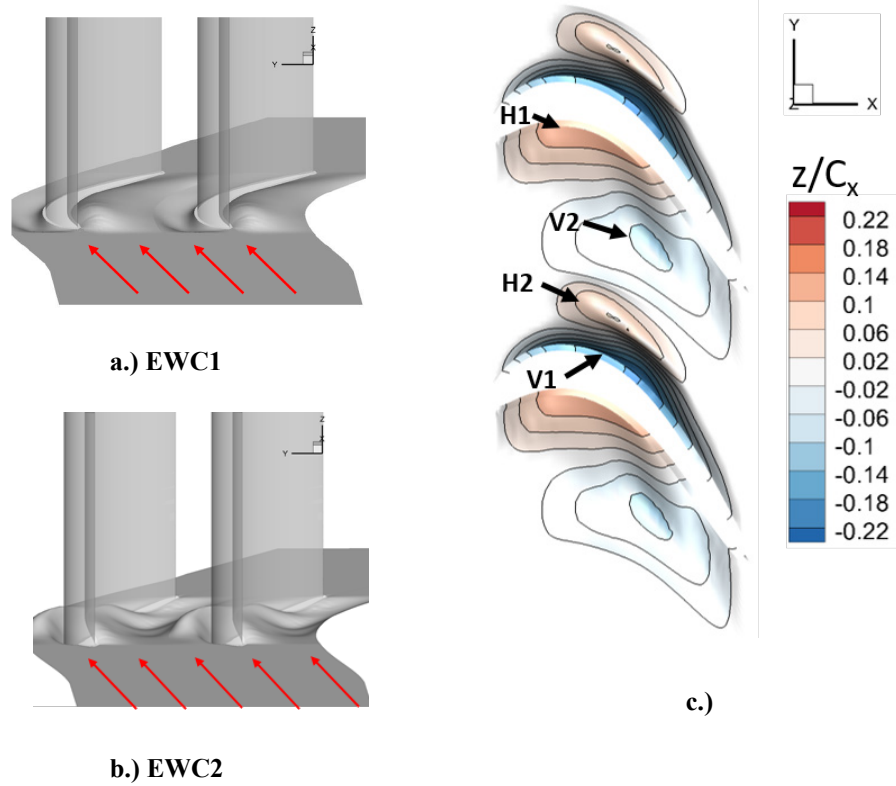


Figure 13 a.) Baseline endwall contour EWC1 compared with b.) GA optimized endwall contour EWC2 c.) EWC2 endwall height with significant topological features labeled as either a hill or valley.

Significant topological features of the contour are labeled hill 1 and 2 (H1, H2), and valley 1 and 2 (V1, V2). The minimum and maximum displacement amplitudes for the contour shape are 22.5% and 14.2% axial chord respectively. These values are within the specified optimization bounds of $\pm 25\%$ axial chord of surface deformation in the spanwise direction normal to the endwall. The two most striking features are V1 and H2. V1 developed into a deep valley along the suction surface, while H2 developed into a streamlined protrusion that could be described as either a fence-like structure or small mid-passage blade. The feature H1 along the pressure side of the passage is similar to the profile contouring shape developed and described in Lyall et al. [13]. Praisner et al. [22] describe a non-axisymmetric endwall contour for a front loaded high-lift profile developed using an automated gradient-based optimization routine. Similarity between the endwall contour described in Ref. [22] and EWC2 is most evident along the pressure surface with both optimizations resulting in hill-like features just downstream from the blade leading edges. The two contour shapes differ significantly along the suction side of the passage.

VI. Discussion of Computational Results

The major endwall flow structures and the influence of each contour on the flowfield are visualized in Figure 14 using isosurfaces of Q and streamlines seeded at three different heights in the incoming boundary layer.

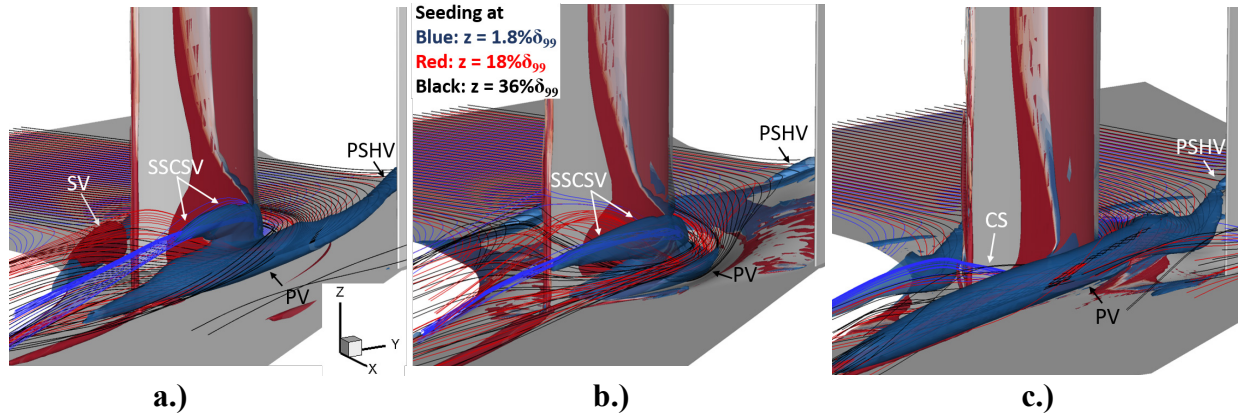


Figure 14 Iso-surfaces of $Q = 10$ colored by secondary vorticity rotational direction, with streamlines seeded in the boundary layer a.) planar endwall b.) EWC1 c.) EWC2.

The prediction of the endwall vortical structures of the baseline case (Figure 14a) by the three-dimensional RANS simulation can be compared with the ILES [28] shown in Figure 1. The most significant secondary flow features, the PSHV, PV, SSCSV, and SV can be identified with a good overall agreement in location. However, the RANS simulation underpredicts the rotational strength of the vortical features compared to the ILES. The vortical features are responsible for generating a large portion the losses through and downstream of the passage. The accurate prediction by the RANS flow solver of the major loss generating features provides confidence that the endwall shapes generated by the numerical model will yield significant reduction in the flow losses.

Compared with the baseline planar endwall the EWC1 shape significantly changes the trajectory of the PSHV. In the contoured case the endwall boundary layer separation line moves upstream in the passage (not shown) with a reduced pressure gradient resulting in a significant reduction in the PSHV strength. The strong corner separation and SSCSV along the suction surface remains. The blue streamlines originate in the low momentum flow located closest to the wall. Figures 14a and 14b show that the low fluid in the incoming boundary layer rolls up into the SSCSV. The vortical structure remains closer to the endwall and is a stronger, tighter vortical structure with the EWC1 shape.

The numerical model of the GA optimized EWC2 shape predicted significant changes to the endwall flow compared to EWC1. In contrast to EWC1, the PSHV is visible and extends into the passage similar to the planar case. However, the hills (H1 and H2) and valley (V2) features work to keep the three-dimensional vortical structure (marked PV) from interacting directly with the suction surface flow and it exits as a strong rotational structure. In the simulation the PV climbed over H2 as it moved through the passage, but was prevented from interacting with the flow near the suction surface. Chung et al. showed similar interactions with the implementation of an endwall fence [10]. The reduced interaction of the PV with the suction surface flow causes loss generation in the corner region to be greatly reduced. Another major effect of the EWC2 shape is the significant reduction in the extent of the suction surface corner separation (marked CS) and elimination of the SSCSV. The curved hill and deep valley features (H2 and V1) located along

the suction surface minimize the roll-up of the low momentum flow in the incoming boundary layer (blue and red streamlines) reducing separation. It is also notable that the trailing edge SV strength is drastically reduced and is no longer visible in both the EWC1 and EWC2 simulations.

Both contour shapes were designed to minimize integrated total pressure loss coefficient. The total pressure loss distribution in the $C_x = 95\%$ and 125% planes are plotted together with isosurfaces of $Q = 10$ in Figure 15. In the baseline planar case, total pressure loss in the corner separation region and in the region of the PV accounts for a significant portion of the loss generation in the passage. The numerical predicted total pressure loss coefficient distribution in the downstream plane ($C_x = 150\%$) are compared in Figure 16.

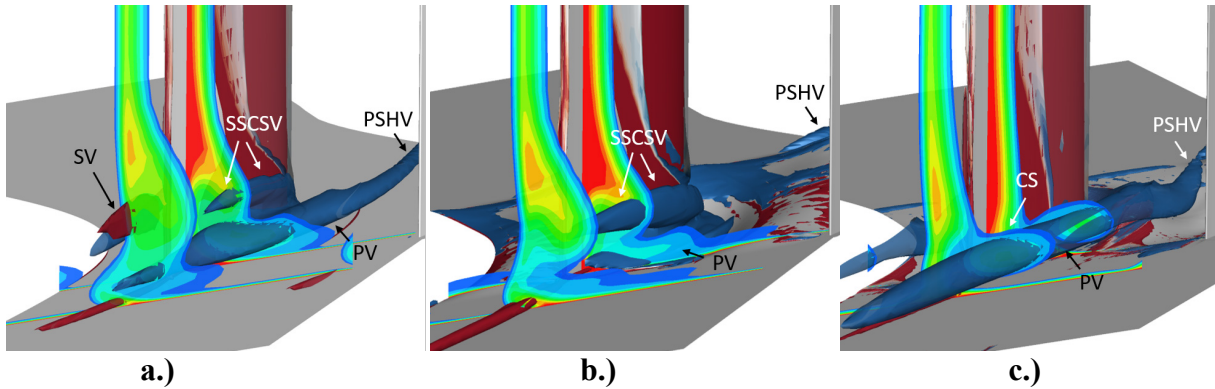


Figure 15 Numerical predictions of total pressure loss coefficient distribution plotted with isosurfaces of $Q = 10$ for a.) planar, b.) EWC1, c.) EWC2.

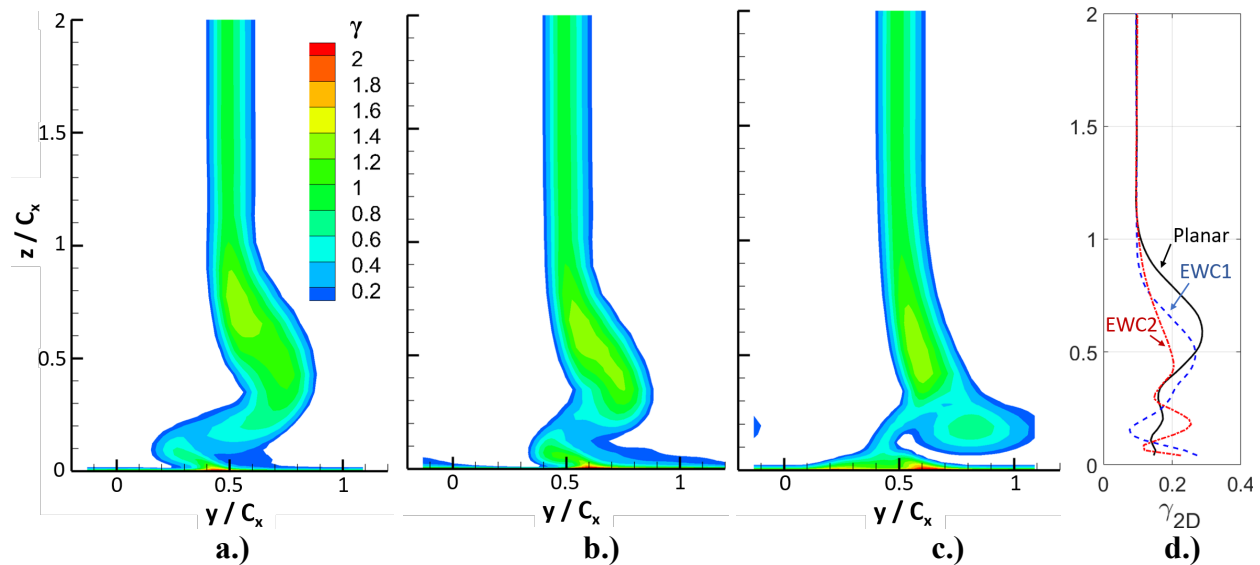


Figure 16 Downstream loss distribution in the $150\% C_x$ plane a.) planar endwall b.) EWC1 c.) EWC2 d.) pitchwise integrated wake total pressure loss coefficient.

The pitchwise integrated loss along the span, shown in Figure 14d, highlights the overall reduction in the penetration height of the endwall flow away from the wall when the endwall contours were used. The reduction in integrated passage total pressure loss predicted for the

EWC1 was 8.2% compared with 10.6% for the GA optimized contour shape EWC2. These values are substantial given the relatively thin incoming boundary layer thickness and large blade aspect ratio used in the simulation.

The effect of the integrated loss can be described by using Figure 16d to designate two loss cores along the span, an upper and a lower. For example, in the planar case the upper loss core is centered around $z/C_x = 0.6$ and coincides with the suction surface corner separation, SSCSV and CV; while the lower loss core centered around $z/C_x = 0.2$ is associated with the passage vortex. Figures 15 and 16 illustrate how the aggressive contouring of the EWC2 resulted in a substantial change in the shape of the endwall loss distribution when compared to the planar case and the L2F-EWC1. In the case of the EWC2 the upper loss core was substantially reduced and narrower due to a decrease in the extent of the suction surface corner separation. The change in the position and interaction of the PV with the suction surface flow leads to an elliptical region of elevated loss located close to the endwall. In terms of integrated values - Figure 16d indicates that there was a significant reduction in loss generation along the upper loss core, whereas, there was an increase in the loss generated in the lower loss core. This observation is different than the EWC1 shape, which lowered the upper loss core spatially while significantly reducing the magnitude of the lower loss core.

Comparing the results of the GA optimized contour EWC2 with the EWC1 leads to the following observation: the two contours work by attacking two different endwall loss production mechanisms. The EWC1 shape primarily reduced the loss associated with PV with minimal effect on the losses generated near the corner separation. In contrast, the EWC2 minimized the interaction between the suction side corner separation and PV. It did not reduce the losses associated with the PV to the same degree as the EWC1, but the losses from the corner separation and SSCSV were essentially eliminated. In future work, additional constraints could be added to the optimization algorithm that focus on reducing the size and strength of the remaining PV to further reduce the losses.

VII. Discussion of Experimental Results

Experimental verification of the endwall contours was completed in the low speed linear cascade wind tunnel. Total pressure loss distribution was measured in two dimensional planes using an inline Kiel probe. The measurement planes of each endwall case are plotted together and are compared in Figure 17.

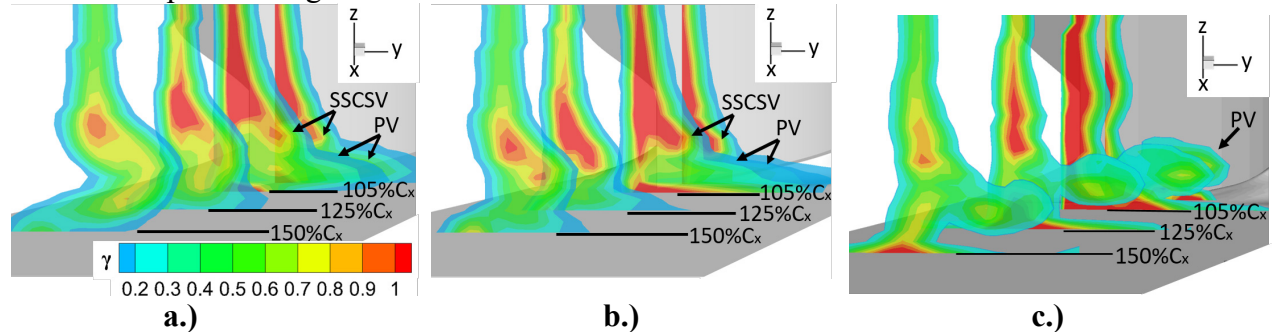


Figure 17 Experimental total pressure loss coefficient distribution through the exit and downstream of the passage for the a.) planar b.) EWC1 c.) EWC2 endwall shapes.

Comparing the EWC1 loss distribution with the planar case shows that the region of loss associated with the suction side corner separation has increased in strength in the case of the EWC1; however, the size and loss associated with the passage vortex has decreased. The weaker PV reduces the spanwise penetration of the endwall losses resulting in two loss cores in the furthest downstream plane that are close to the endwall. The development of total pressure loss in the case of the EWC2 shape was drastically different than the planar case. The loss region associated with the PV is distinguished as an oval region that slowly mixes with the rest of the wake loss as it exits the passage. The significant losses associated with the corner separation observed in the planar and EWC1 cases did not exist in the optimized case. This agrees with the numerical simulation. The H2 feature keeps the PV away from the suction surface, while significant shaping such as valley V1 along the suction surface significantly weakens the corner separation and interaction of the PV with the suction surface flow.

The reduction in the integrated passage total pressure loss coefficient measured in the experiments were 7.8% using the EWC1 shape and 8.6% using the GA optimized EWC2. Both measured values were lower than the numerical predictions: 5% less for the EWC1 and 19% lower than predicted for the more radical EWC2 shape. The relatively small difference in measured and predicted loss reduction is quite good given the documented challenges associated with predicting three-dimensional endwall losses using RANS simulations (see, e.g., Ref. 4). The pitchwise integrated total pressure loss measurements of the baseline and GA optimized EWC2 are compared in Figure 18.

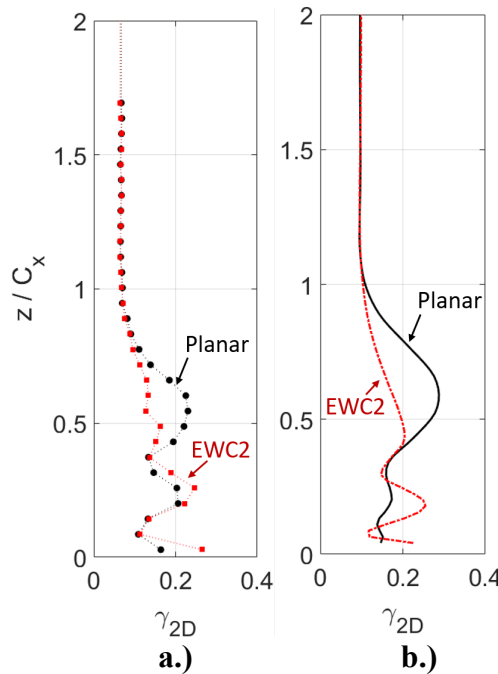


Figure 18 Pitchwise integrated wake total pressure loss coefficient in the 150% C_x plane a.) experiment b.) computational model.

In the planar case, the simulations under predict the total pressure loss in the lower loss core associated with the PV and over predict the penetration of the endwall losses into the passage. However, in the case of the EWC2 shape the numerical simulation accurately predicted a significant decrease in the upper loss core associated with the suction surface corner separation and increase in the losses in the lower loss core.

The measured and predicted total pressure loss distribution of the EWC2 contour in the 85%, 95%, 105%, 125%, and 150% C_x planes are compared in Figure 19.

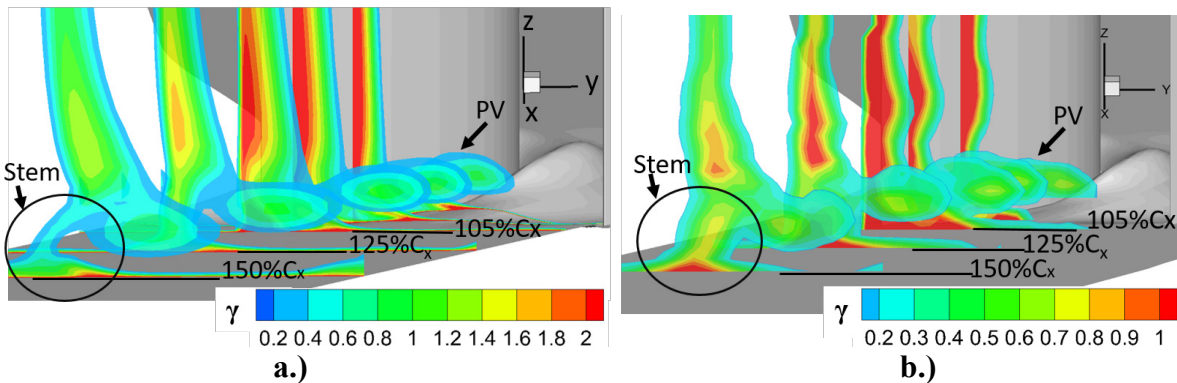


Figure 19 EWC2 total pressure loss coefficient distribution through the exit and downstream of the passage for a.) computational simulation and b.) experimental.

Similarities are prevalent with good agreement of the simulation with respect to the shape and position of the PV loss region, which stays relatively close to the endwall when exiting the passage. The most notable difference between the RANS and experimental data was the region marked “stem” extending from the endwall up to the PV loss core. This region is associated with a counter-rotating vortex along the hill H2 and corner vortex at the junction of the blade and

endwall. The stem was significantly thicker and has a relatively higher loss value in the experiment and was under predicted in the simulation.

Finally, to determine the sensitivity of the GA optimized contour shape, additional experimental measurements of passage total pressure loss were obtained after slightly altering two of the key shape features. Each shape variation was made independent from one another to test each feature's sensitivity. The first feature investigated was the large valley, V1, on the suction side of the passage. The overall depth of the feature was reduced $8.3\%C_x$ by adding filler material to the valley. There was still a substantial valley after decreasing the depth from the optimized value. The resulting effect on the integrated passage loss was a reduced benefit from the contour. The second shape sensitivity investigated was an extension to the hill H2 in an attempt to keep the PV further away from the suction surface. This too resulted in a decreased benefit from the endwall contour. The EWC2 shape was extreme when compared with those in the literature, but these sensitivity experiments provide confidence that the contour was near an optimum in the design space.

While the RANS simulations are unable to precisely predict either the profile or endwall loss distribution, the agreement between simulation and experiment is good, especially with respect to predicting the overall changes to the three-dimensional flow structures due to endwall shaping. The simulations provided enough fidelity to predict the large scale changes to the endwall flow and insight into the mechanism that led to the loss reduction. The experimental verification shows that the computational tools and overall optimization workflow described are capable of designing endwall contour shapes using total pressure loss as a cost function.

VIII. Conclusions

High-lift low-pressure turbine passages typically have high losses in the endwall region. Two different endwall contours were designed for the high-lift front loaded L2F research profile. The first shape (EWC1) was developed to verify a new RANS based design workflow, which in addition to the computational flow solver, used a set of Bezier curves and a mesh morphing module to design the endwall contours. EWC1 could be described as having similar hill and valley features as previous non-axisymmetric endwall contours described in the literature. The second shape was developed using a genetic algorithm to find an optimal contour based on the predicted total pressure loss reduction compared to a flat planar endwall. The EWC1 had a significantly lower magnitude of contouring compared to the aggressive EWC2 endwall contour shape. The EWC2 included a hill along the blade pressure side, a large streamline hill in the passage, and a deep valley along the junction of the endwall and blade suction surface.

The computational models predicted the EWC1 and EWC2 shapes would result in an 8.2% and 10.6% reduction in the integrated total pressure loss respectively. The two contours were experimentally tested in a low-speed wind tunnel producing 7.8% and 8.6% reductions in loss compared to the planar endwall. While the numerical predictions did not precisely predict the passage total pressure loss reduction in each case, it showed good agreement with the experimental two-dimensional loss distribution through the passage, and the positional changes of the most significant endwall flow structures.

One of the most interesting outcomes was the difference in the mechanism responsible for the loss reductions measured with the EWC1 and EWC2 shapes. With the more traditional EWC1 shape, the loss associated with the suction side corner separation and vortex (SSCSV) was slightly higher, while the passage vortex and associated loss was lower. This resulted in a reduction in integrated total pressure loss and less penetration of the low momentum endwall flow into the passage away from the endwall. In the case of the GA optimized EWC2 shape, the sharp valleys and mid-passage ridge minimized the suction surface corner separation and the passage vortex remained separated from suction surface. The positional change of the passage vortex decreased interaction with suction surface flow reducing loss. The relationship between endwall loss reduction and passage vortex proximity to the blade suction surface flow is consistent with prior active jet blowing experiments using the same blade profile described by Benton et al. [5]. Finally, the deep valley and ridge of the optimal EWC2 shape were modified slightly in the linear cascade to investigate the sensitivity of the shape of the features on the loss reduction. All modifications to the endwall contour resulted in a reduced performance compared to the optimal contour. Therefore, the experimental results verified that the numerical model and workflow were able to develop an optimal endwall shape configuration based on the chosen cost function.

Design approaches that optimally shape both the blade profile and endwall contour will be most effective at reducing endwall loss through the passage. While low speed linear cascades are useful for numerical tool development and fundamental aerodynamic studies, future work will need to consider heat transfer and the effects of compressibility and unsteady flows to move forward with improved high-lift turbine designs.

Funding Sources

This paper has been cleared for public release, case number: 88ABW-2019-4829. Authors 1-3 were supported by the Air Force Office of Scientific Research under award number FA9550-18RQCOR063. Author 4 was supported by the Air Force Research Laboratory and Southwestern Council for Higher Education under agreement FA8650-12-2-7248. Any opinions, findings, and conclusions or recommendations expressed in this material are those of the author(s) and do not necessarily reflect the views of the United States Air Force.

Acknowledgements

The authors would like to acknowledge Dr. John Clark for his assistance and insight into the development of the design tools and optimization routine used in the present study.

References

- [1] Howell, R. J., Hodson, H. P., Schulte, V., Stieger, R. D., Schiffer, H., Haselbach, F., and Harvey, N. W., "Boundary Layer Development in the BR710 and BR715 LP Turbines—The Implementation of High-Lift and Ultra-High-Lift Concepts," *Journal of Turbomachinery*, Vol. 124, No. 3, July 2002, pp. 385-392. <https://doi.org/10.1115/1.1457455>
- [2] Praisner, T. J., Grover, E. A., Knezevici, D. C., Popvic, I., Sjolander, S. A., Clark, J. P., Sondergaard, R., "Toward Expansion of the Low-Pressure-Turbine Airfoil Design Space," *Journal of Turbomachinery*, Vol. 135, No. 6, Sep. 2013. <https://doi.org/10.1115/1.4024796>
- [3] McQuilling, M., "Design and Validation of a High-Lift Low-Pressure Turbine Blade," Ph.D. Dissertation, Wright State University, 2007.
- [4] Schmitz, J. T., Morris, S. C., Ma, R. R., Corke, T. C., Clark, J. P., Koch, P. J., Puterbaugh, S. L., "Highly Loaded Low-Pressure Turbine: Design, Numerical, and Experimental Analysis," American Society of Mechanical Engineers, Paper GT2010-23591, June 2010. <https://doi.org/10.1115/1.4024796>
- [5] Benton, S., Bernardini, C., Bons, J., and Sondergaard, R., "Parametric Optimization of Unsteady End Wall Blowing on a Highly Loaded Low-Pressure Turbine," *Journal of Turbomachinery*, Vol. 136, No. 7, Jan. 2014. <https://doi.org/10.1115/1.4026127>
- [6] Bons, J., Benton, S., Bernardini, C., Bloxham, M., "Active Flow Control for Low-Pressure Turbines," *AIAA Journal*, Vol. 56, No. 7, 2018, pp. 2687-2698. doi: 10.2514/1.J056697
- [7] Fletcher, N., Wolff, M., Marks, C. R., Petrie, R., Sondergaard, R., "Experimental Investigation of Endwall Flow Control for Front-Loaded Turbine Blades," AIAA Paper 2018-4436, 2018. doi: 10.2514/6.2018-4436
- [8] Kawai, T., Shinoki, S., and Adachi, T., "Secondary Flow Control and Loss Reduction in a Turbine Cascade Using Endwall Fences," *JSME International Journal*, Series II, Vol. 32, No. 3, 1989. https://doi.org/10.1299/jsmeb1988.32.3_375
- [9] Kawai, T., Shinoki, S., Adachi, T., "Visualization Study of Three-Dimensional Flows in a Turbine Cascade Endwall Region," *JSME International Journal*, Series II, Vol. 33, No. 2, 1990. https://doi.org/10.1299/jsmeb1988.33.2_256
- [10] Chung, J. T., Simon, T. W., Buddhavarapu J. J., "Three-Dimensional Flow Near the Blade/Endwall Junction of a Gas Turbine: Application of a Boundary Layer Fence," American Society of Mechanical Engineers, Paper 91-GT-045, 1991. doi: 10.1115/91-GT-045
- [11] Aunapu, N. V., Volino, R. J., Flack, K. A., Stoddard, R. M., "Secondary Flow Measurements in a Turbine Passage with Endwall Flow Modification," American Society of Mechanical Engineers, Paper 2000-GT-0212, 2000. <https://doi.org/10.1115/2000-GT-0212>
- [12] Sauer, H., Muller, R., Vogeler, K., "Reduction of Secondary Flow Losses in Turbine Cascades by Leading Edge Modifications at the Endwall," *Journal of Turbomachinery*, Vol. 123, No. 2, Feb. 2000, pp. 207-213. <https://doi.org/10.1115/1.1354142>
- [13] Lyall, M. E., King P. I., Clark, J. P., Sondergaard, R., "Endwall Loss Reduction of High Lift Low Pressure Turbine Airfoils Using Profile Contouring—Part I: Airfoil Design," *Journal of Turbomachinery*, Vol. 136, No. 8, Jan. 2014. doi: 10.1115/1.4025951
- [14] Sangston, K., Little, J., Lyall, M., and Sondergaard, R., "Endwall Loss Reduction of High Lift Low Pressure Turbine Airfoils Using Profile Contouring—Part II: Validation", *Journal of Turbomachinery*, Vol. 136, No. 8, Jan. 2014. doi: 10.1115/1.4025952

- [15] Bear, P., Wolff, M., Gross, A., Marks, C. R., Sondergaard, R., “Experimental Investigation of Total Pressure Loss Development in a Highly Loaded Low Pressure Turbine Cascade,” *Journal of Turbomachinery*, Vol. 140, No. 3, March 2018. doi: 10.1115/1.4038413
- [16] Atkins, M.J., “Secondary losses and end-wall profiling in a turbine cascade,” I.Mech.E. Turbo-Conference, Paper C255/87, 1987.
- [17] Rose, M.G., “Non-axisymmetric Endwall Profiling in the HP NGV’s of an Axial Flow Gas Turbine,” American Society of Mechanical Engineers, Paper 94-GT-249, June 1994. <https://doi.org/10.1115/94-GT-249>
- [18] Yan, J., Gregory-Smith, D. G., and Walker, P. J., “Secondary Flow Reduction in a Nozzle Guide Vane by Non-Axisymmetric End-Wall Profiling,” American Society of Mechanical Engineers, Paper 99-GT-339, June 1999. <https://doi.org/10.1115/99-GT-339>
- [19] Harvey, N. W., Rose, M. G., Taylor, M. D., Shahpar, S., Hartland, J. C., and Gregory-Smith, D. G., “Nonaxisymmetric Turbine End Wall Design: Part I—Three-Dimensional Linear Design System,” *Journal of Turbomachinery*, Vol. 122, No. 2, Feb. 1999, pp. 278-285. <https://doi.org/10.1115/1.555445>
- [20] Knezevici, D. C., Sjolander, S. A., Praisner, T. J., Allen-Bradley, E., and Grover, E.A., “Measurements of Secondary Losses in a Turbine Cascade With the Implementation of Non-Axisymmetric Endwall Contouring,” American Society of Mechanical Engineers, Paper GT2008-51311, Jan. 2008. <https://doi.org/10.1115/GT2008-51311>
- [21] Knezevici, D. C., Sjolander, S. A., Praisner, T. J., Allen-Bradley, E., and Grover, E. A., 2009, “Measurements of Secondary Losses in a High-Lift Front-Loaded Turbine Cascade With the Implementation of Non-Axisymmetric Endwall Contouring,” American Society of Mechanical Engineers, Paper GT2009-59677, Jan. 2009. <https://doi.org/10.1115/GT2009-59677>
- [22] Praisner, T.J., Allen-Bradley, E., Grover, E.A., Knezevici, D.C., and Sjolander, S.A., "Application of Nonaxisymmetric Endwall Contouring to Conventional and High-Lift Turbine Airfoils," *Journal of Turbomachinery*, Vol. 135, Nov. 2013. <https://doi.org/10.1115/1.4024023>
- [23] Langston L. S., "Secondary Flows in Axial Turbines—A Review," *Annals of the New York Academy of Sciences*, Vol. 934, No. 1, 2001, pp. 11-26. <https://doi.org/10.1111/j.1749-6632.2001.tb05839.x>
- [24] Sharma OP, Butler TL. Predictions of Endwall Losses and Secondary Flows in Axial Flow Turbine Cascades. *Journal of Turbomachinery*, Vol. 109, No. 2, Apr. 1987, pp. 229-236. doi: 10.1115/1.3262089
- [25] Dickel, J., Marks, C., Clark, J., Sondergaard, R., and Wolff, M., “Non-Axisymmetric Endwall Contouring of Front-Loaded- High-Lift Low Pressure Turbines,” AIAA Paper 2018-0114, Jan. 2018. <https://doi.org/10.2514/6.2018-2125>
- [26] Marks, C. R., Sondergaard, R., Bear, P. S., Wolff, M., “Reynolds Number Effects on the Secondary Flow of Profile Contoured Low Pressure Turbines,” AIAA Paper 2016-0114, Jan. 2016. <https://doi.org/10.2514/6.2016-0114>
- [27] Bear, P., Wolff, M., Gross, A., Marks, C. R., Sondergaard, R., “Secondary Loss Production Mechanisms in a Low Pressure Turbine Cascade,” AIAA Paper 2016-4554, July 2016. <https://doi.org/10.2514/6.2016-4554>
- [28] Gross, A., Marks, C. R., Sondergaard, R., Bear, P., Wolff, J. M., “Experimental and Numerical Characterization of Flow through Highly Loaded Low-Pressure Turbine

- Cascade,” *Journal of Propulsion and Power*, Vol. 34, No. 1, 2018, pp. 27-39.
<https://doi.org/10.2514/1.B36526>
- [29] Ni, R. H., Humber, W., Fan, G., Johnson, P. D., Downs, J., Clark, J. P., Koch, P. J., "Conjugate Heat Transfer Analysis of a Film-Cooled Turbine Vane," American Society of Mechanical Engineers, Paper GT2011-45920, 2011. <https://doi.org/10.1115/GT2011-45920>
- [30] Wilcox, D. C., *Turbulence Modeling for CFD*, 2nd Edition, DCW Industries Inc., La Canada, California, 1998.
- [31] Lyall, M. E., "Effects of Front-Loading and Stagger Angle on Endwall Losses in High Lift Low Pressure Turbine Vanes," Ph.D. Dissertation, Air Force Institute of Technology, 2012.
- [32] Hirsch, C., *Numerical Computation of Internal & External Flows – The Fundamentals of Computational Fluid Dynamics*, 2nd Edition, p. 596, Elsevier, Oxford, UK, 2007.
- [33] Johnson, J., King, P., Clark, J., and Ooten, M., "Design Optimization Methods for Improving HPT Vane Pressure Side Cooling Properties Using Genetic Algorithms and Efficient CFD," AIAA Paper 2012-326, Jan. 2012. <https://doi.org/10.2514/6.2012-326>
- [34] Kaszynski, A. A., Beck, J. A., Brown, J. M., "Experimental Validation of a Mesh Quality Optimized Morphed Geometric Mistuning Model," American Society of Mechanical Engineers, Paper GT2015-43150, 2015. <https://doi.org/10.1115/GT2015-43150>
- [35] Arora, J. S., *Introduction to Optimum Design*, Elsevier Academic Press, San Diego, CA, 2004. <https://doi.org/10.1016/B978-012064155-0/50004-5>

Nomenclature

C_x = axial chord

C_p = pressure coefficient

H = span

P_s = static pressure

P_t = total pressure

Q = Q-criterion

Re = Reynolds number based on inlet velocity and axial chord

S = pitch

Z_w = Zweifel loading coefficient

γ = total pressure loss coefficient

γ_{ps} = area averaged passage total pressure loss coefficient

γ_{2D} = area averaged total pressure loss coefficient across one pitch

δ_{99} = boundary layer thickness

λ = transformed spanwise direction

ξ = transformed pitch direction

ρ = density

χ = transformed chord direction